



Showcasing research from Professor Zhengtao Deng's laboratory, College of Engineering and Applied Sciences, Nanjing University, Jiangsu, P.R. China.

Solid-state synthesis of cesium manganese halide nanocrystals in glass with bright and broad red emission for white LEDs

Ultra-stable CsMnX_3 ($X = \text{Cl}, \text{Br}, \text{I}$) nanocrystals embedded in borosilicate glasses with a stable photoluminescence (PL) emission maximum at 649 nm, high PL quantum yield of 65.1%, and wide line-width of 130 nm were synthesized as excellent red phosphors for white light-emitting diode (LED) devices with a high color rendering index (CRI).


As featured in:



See Zhengtao Deng *et al.*,
Chem. Sci., 2023, **14**, 5309.

Cite this: *Chem. Sci.*, 2023, 14, 5309 All publication charges for this article have been paid for by the Royal Society of Chemistry

Solid-state synthesis of cesium manganese halide nanocrystals in glass with bright and broad red emission for white LEDs†

Guangyong Xu, Chuying Wang, Yacong Li, Wen Meng, Guigen Luo, Min Peng, Bin Xu and Zhengtao Deng *

Recently, lead halide perovskite nanocrystals (NCs) have attracted extensive attention due to their unique optical properties. However, the toxicity of lead and the instability to moisture obstruct their further commercial development. Herein, a series of lead-free CsMnX_3 ($\text{X} = \text{Cl}, \text{Br}, \text{and I}$) NCs embedded in glasses were synthesized by a high temperature solid-state chemistry method. These NCs embedded in glass can remain stable after soaking in water for 90 days. It is found that increasing the amount of cesium carbonate in the synthesis process can not only prevent the oxidation of Mn^{2+} to Mn^{3+} and promote the transparency of glass in the 450–700 nm region, but also significantly increase its photoluminescence quantum yield (PLQY) from 2.9% to 65.1%, which is the highest reported value of the red CsMnX_3 NCs so far. Using CsMnBr_3 NCs with a red emission peak at 649 nm and full-width-at-half-maximum (FWHM) of 130 nm as the red light source, a white light-emitting diode (LED) device with International Commission on illumination (CIE) coordinates of (0.33, 0.36) and a color rendering index (CRI) of 94 was obtained. These findings, together with future research, are likely to yield stable and bright lead-free NCs for the next generation of solid-state lighting.

Received 27th February 2023

Accepted 15th April 2023

DOI: 10.1039/d3sc01084h

rsc.li/chemical-science

Introduction

Lead halide perovskite nanocrystals (NCs) have excellent optical properties, including a high photoluminescence quantum yield (PLQY), narrow emission peak, and high emission color tunability.^{1–5} As a result, they are being studied for a wide range of applications, such as light-emitting diodes (LEDs), luminescent solar concentrators (LSCs), displays, and solid-state lighting.^{6–9} However, lead halide perovskite NCs are easily decomposed by water, oxygen, and heat, so the stability is poor in the working environment, which is not conducive to practical application.^{10,11} Therefore, various strategies including compositional regulation, shell growth, defect passivation, and polymer encapsulation have been developed to improve their stability.^{12–16} Considering the robust and inert structure of glass, *in situ* crystallization of CsPbX_3 ($\text{X} = \text{Cl}, \text{Br}, \text{and I}$) NCs in glass is considered to be one of the most effective methods. The stability of CsPbX_3 NCs was significantly improved by embedding them in glass.^{17–19}

On the other hand, as a result of concerns about Pb toxicity, research to develop lead-free NCs has progressed significantly in

recent years.¹⁰ Considering that Sn^{2+} , Ge^{2+} , and Pb^{2+} have similar extranuclear electronic configurations, replacing Pb^{2+} with Sn^{2+} and Ge^{2+} has been studied.²⁰ However, Sn^{2+} and Ge^{2+} are easily oxidized when exposed to air at high temperature, resulting in increasing internal defects and a low rate of radiation recombination.^{21,22} Recently, manganese (Mn) halides have attracted great attention because of their low toxicity, rich earth content and low cost.^{23–25} More importantly, the emissions of Mn^{2+} -based metal halides can change from green to red by changing the coordination number of Mn^{2+} ions.²⁶ Generally, Cs_3MnX_5 shows green emission with tetrahedrally coordinated Mn^{2+} ions, while CsMnX_3 exhibits wide red emission with octahedrally coordinated Mn^{2+} ions.^{27–29} For lighting applications, the ideal white light source should emit a continuous and broad spectrum like natural sunlight,^{30,31} and therefore, the wide red emission is beneficial for solid-state lighting. Unfortunately, the PLQY of red emission Mn^{2+} -based metal halides is much lower than that of green emission. This is because the small Mn–Mn distance plays an important role in PL quenching of the Mn^{2+} ion luminescence centre in octahedral CsMnX_3 .²⁸ Therefore, it is important to develop a new strategy to improve the PLQY of manganese halide NCs.

It is important to note that Mn^{2+} -based metal halide NCs are also sensitive to humidity, oxygen, and heat, which limits their practical application. For instance, for cesium manganese halides, a phase transition can easily occur and lead to the formation of weak luminescence phases such as $\text{Cs}_2\text{MnBr}_4 \cdot 2\text{H}_2\text{O}$

College of Engineering and Applied Sciences, State Key Laboratory of Analytical Chemistry for Life Science, National Laboratory of Microstructures, Nanjing University, Nanjing, Jiangsu, 210023, P. R. China. E-mail: dengz@nju.edu.cn

† Electronic supplementary information (ESI) available: Photographs of CsMnBr_3 NC embedded glasses; absorption spectra, PL spectra, PLE spectra and photoluminescence decay curves. See DOI: <https://doi.org/10.1039/d3sc01084h>

and $\text{CsMnCl}_3 \cdot 2\text{H}_2\text{O}$ in a humid environment.^{28,32} Thus, the PLQYs of as synthesized samples are always low. Very recently, Liu *et al.* reported CsMnX_3 NC embedded glass with the highest PLQY of 41.8% (CsMnCl_3) for X-ray imaging.³³ However, there are obvious absorption peaks in the 500–550 nm region of the UV-vis absorption spectra of the CsMnX_3 NCs, indicating the existence of Mn^{3+} .³⁴ Therefore, it is urgent to develop new methods to improve the stability of manganese halide NCs.

In this study, combining the advantages of the inorganic glass matrix and lead-free manganese halide materials, CsMnX_3 ($\text{X} = \text{Cl}, \text{Br}, \text{and I}$) NCs were *in situ* precipitated in glass using a high temperature solid-state chemistry method. The oxidation of Mn^{2+} to Mn^{3+} during the synthesis was prevented by increasing the content of cesium carbonate, which not only results in a significant improvement in PLQY from 2.9% to 65.1%, but also greatly improves the transparency of the samples in the 450–700 nm region. More importantly, cesium manganese halide nanocrystal embedded glasses exhibit outstanding long-term stability against water owing to the dense glass network. Using the highly stable CsMnBr_3 NCs in glass as the broad red emitter, white LEDs with International Commission on illumination (CIE) coordinates of (0.33, 0.36) and a high color rendering index (CRI) value of 94 were obtained.

Results and discussion

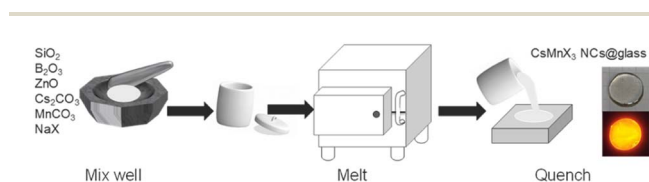
Generally speaking, the chemical durability and thermal stability of borosilicate glasses are much better than those of normal borogermanate, phosphate and tellurite glasses, considering their glass transition temperature and network structure.^{18,19} So borosilicate glasses with a composition of $15\text{SiO}_2\text{--}30\text{B}_2\text{O}_3\text{--}10\text{ZnO}$ (in mol%) were selected as the glass matrix. Herein, ZnO was used as a flux to reduce the melting point of the system.³⁵ As shown in Scheme 1, CsMnBr_3 NC embedded glasses were prepared by a conventional melt-quenching method. As shown in Fig. 1a, the obtained CsMnBr_3 NC embedded glasses exhibit bright red-emission under UV irradiation, indicating that Mn^{2+} is octahedrally coordinated. Absorption peaks induced by Mn^{2+} , ${}^6\text{A}_1 \rightarrow {}^4\text{E}(\text{D})$ transition and ${}^6\text{A}_1 \rightarrow {}^4\text{A}_1, {}^4\text{E}_1(\text{G})$ transition, are observed at 365 and 412 nm (Fig. 1a). It should be noted that no absorption feature was found in the 450–700 nm region, indicating the high transparency and absence of Mn^{3+} oxidized species observed before.³³ The emission spectrum of the CsMnBr_3 NCs exhibits a broad red emission peak centered at 649 nm with a FWHM of 130 nm (Fig. 1b). The red PL emission is assigned to the ${}^4\text{T}_1 \rightarrow {}^6\text{A}_1$ transition in the $[\text{MnBr}_6]^{4-}$ octahedron of the CsMnBr_3 nanocrystals, which is consistent with the

reported red emission from Mn^{2+} in the $[\text{MnBr}_6]^{4-}$ octahedron.²⁸ For comparison, the absorption and emission properties of the glass matrix (blank group) are shown in Fig. S1.† Similarly, there is no absorption feature found in the 450–700 nm region. But there is no emission observed in the blank group under UV light. More importantly, the PLQY of CsMnBr_3 nanocrystals is up to 65.1%, which is higher than those of Mn^{2+} -based lead-free perovskites previously reported (Fig. 2). In contrast to previous studies,^{28,29,33,36} these CsMnBr_3 nanocrystal embedded glass samples with a larger FWHM are more suitable for solid-state lighting (Fig. 2). The larger FWHM may be ascribed to the glass matrix.^{33,37}

In order to explore the origin of red emission, PL excitation (PLE) spectra are recorded (Fig. 1b). Three typical PLE peaks at 330, 365, and 412 nm are observed, corresponding to the ${}^6\text{A}_1 \rightarrow {}^4\text{E}(\text{D})$, ${}^6\text{A}_1 \rightarrow {}^4\text{T}_2(\text{D})$, and ${}^6\text{A}_1 \rightarrow {}^4\text{A}_1, {}^4\text{E}(\text{G})$ transitions of Mn^{2+} ions in octahedral coordination, respectively. As shown in Fig. 1c, the photoluminescence decay curves of CsMnBr_3 NCs can be well fitted by a double-exponential function, yielding two lifetimes ($t_1 = 1.38 \mu\text{s}$ and $t_2 = 17.32 \mu\text{s}$) with an average lifetime of 6.37 μs . Compared with previous reports that Mn^{2+} -based metal halides exhibit radiative lifetimes of about hundreds of microseconds,^{28,38} the shorter lifetime is more conducive to practical application.

The CsMnBr_3 NCs are further analysed by excitation–emission matrix fluorescence spectroscopy (Fig. 1d). With the change of the excitation wavelength, the emission peaks show no obvious shift, suggesting high quality of our sample. The optical properties are induced by the precipitation of CsMnBr_3 nanocrystals in glasses, which is directly confirmed through TEM analysis (Fig. 1e and f). Nearly spherical CsMnBr_3 nanocrystals are homogeneously precipitated in the glass matrix. The average diameter of these nanocrystals is found to be 3.9 nm (Fig. 1e). As shown in Fig. 1f, a clear lattice spacing of 0.30 nm, corresponding to the (201) lattice plane of hexagonal-structure CsMnBr_3 crystal, is observed.

Bromine content has a significant impact on CsMnBr_3 NCs, which prompted us to conduct more studies on the synthesis of CsMnBr_3 NC embedded glasses. Thus, glasses with different molar ratios between NaBr and MnCO_3 are designed and prepared using the melt-quenching method. As shown in Fig. S2a,† the obtained CsMnBr_3 NC embedded glasses exhibit bright red-emitting under UV irradiation. Fig. S2b† shows the UV-vis absorption spectra of CsMnBr_3 NC embedded glasses with different Br/Mn molar ratios. There is a broad absorption peak from 400 nm to 700 nm for all samples, corresponding to Mn^{3+} .^{34,39} The broad absorption peak gradually weakens with increasing Br/Mn molar ratio, indicating the decrease of Mn^{3+} content. The reason for the decrease of Mn^{3+} content is probably that Br^- is more easily oxidized than Mn^{2+} . Thus, the oxidation degree of Mn^{2+} in the sample with high bromine content is weakened. In addition, absorption peaks induced by Mn^{2+} , ${}^6\text{A}_1 \rightarrow {}^4\text{E}(\text{D})$ transition and ${}^6\text{A}_1 \rightarrow {}^4\text{A}_1, {}^4\text{E}_1(\text{G})$ transition, are also observed at 365 and 412 nm. With the increase of Br/Mn molar ratio, the photoluminescence intensity shows a trend of increasing and then slightly decreasing (Fig. S2c†), which is mainly ascribed to the increase of CsMnBr_3 nanocrystals. Although the oxidation of Mn^{2+} can be weakened by increasing



Scheme 1 Schematic diagram of the synthesis of CsMnX_3 NC embedded glass.



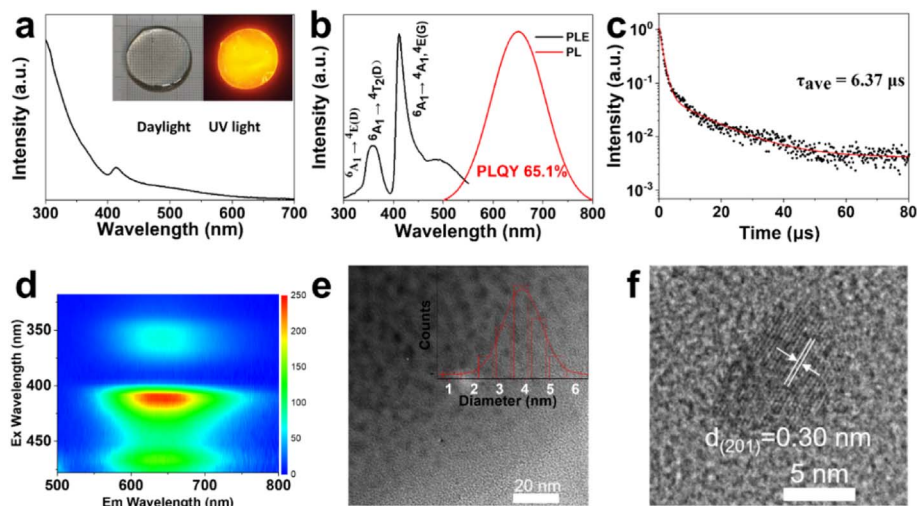


Fig. 1 The optical properties and morphology of the typical CsMnBr_3 NC embedded glass using sample S7 as an example. (a) The UV-vis absorption spectra. Inset shows photographs of a typical CsMnBr_3 NC embedded glass under daylight and UV light. (b) PL emission and PL excitation spectra. (c) PL lifetime decay curve. (d) 3D excitation-emission matrix (EEM) fluorescence spectrum. (e) TEM image. Inset (e) is the size distribution histogram of CsMnBr_3 NCs embedded in glass. (f) HRTEM image of a typical CsMnBr_3 NC.

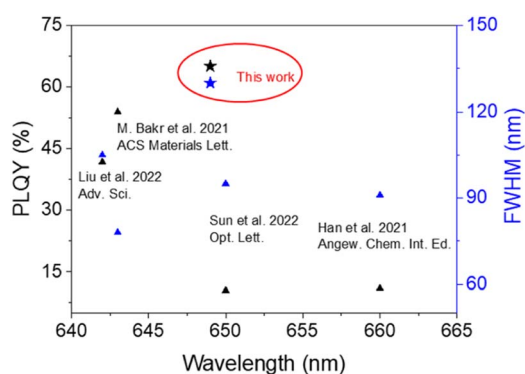


Fig. 2 The summary of the red emissive CsMnX_3 NCs reported so far, indicating the NCs in the current work have the highest PLQY of 65.1% and largest full-width-at-half-maximum (FWHM) of 130 nm. Both of these properties make the NCs reported here particularly suitable as a red fluorescent material for white LED lighting.

the bromine content, it cannot be completely inhibited. Therefore, it is necessary to take further measures to inhibit the oxidation of Mn^{2+} .

Considering that the CO_2 generated by the decomposition of carbonate could eliminate the oxygen in the melt, thereby weakening the oxidation of Mn^{2+} and the Cs/Mn molar ratio will affect the coordination states of manganese ions in the process of synthesizing manganese halide perovskite nanocrystals,^{28,40} glasses with different molar ratios between Cs_2CO_3 and MnCO_3 are prepared on the basis of the optimum bromine/manganese ratio. Interestingly, in our work, the samples with different Cs/Mn ratios still show broad red emission (Fig. 3c), indicating that the coordination state of manganese ions has not changed, and it is still octahedrally coordinated.

As the molar ratio of Cs/Mn increases from 2 : 1 to 4.5 : 1, the color of the samples changes from brown to colourless and

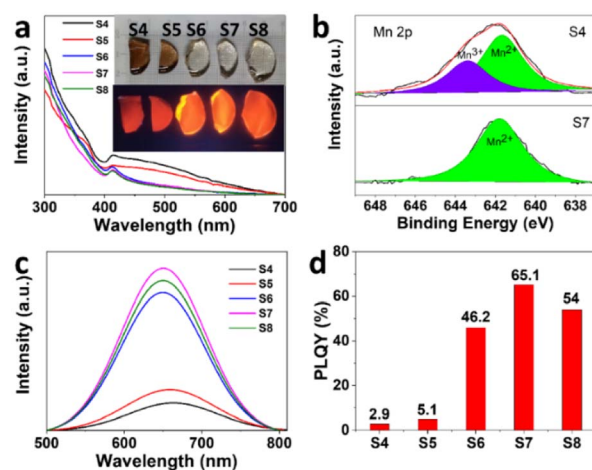


Fig. 3 The influence of the amount of Cs_2CO_3 on the final product of the CsMnBr_3 NC embedded glasses. (a) UV-vis absorption spectra. Inset shows photographs of a series of CsMnBr_3 NC embedded glasses under daylight and UV light. (b) Mn 2p XPS spectra of samples S4 and S7. (c) PL emission spectra and (d) the PLQY of a series of CsMnBr_3 NC embedded glasses with different amounts of Cs_2CO_3 . Note: $15\text{SiO}_2-30\text{B}_2\text{O}_3-10\text{ZnO}-x\text{Cs}_2\text{CO}_3-1\text{MnCO}_3-10\text{NaBr}$ ($x = 1, 1.5, 1.75, 2$, and 2.25 , denoted as S4, S5, S6, S7, and S8).

transparent (Fig. 3a). The origin of brown is Mn^{3+} , derived from the oxidized Mn^{2+} during melting, which is further confirmed by the absorption spectrum and X-ray photoelectron spectroscopy (XPS) analysis (Fig. 3b). While the d-d transitions of Mn^{2+} ions are forbidden, resulting in weak light absorption, this kind of compound with octahedral coordination is typically pale pink to pale to colorless.⁴¹ There is a broad absorption peak from 400 nm to 700 nm for sample S4 and sample S5 (Fig. 3a), which corresponds to Mn^{3+} . While there is no broad absorption peak at the corresponding position for samples S6, S7, and S8, indicating

that there is no Mn^{3+} in the samples. In addition, absorption peaks induced by Mn^{2+} , ${}^6\text{A}_1 \rightarrow {}^4\text{E}(\text{D})$ transition and ${}^6\text{A}_1 \rightarrow {}^4\text{A}_1$, ${}^4\text{E}_1(\text{G})$ transition, are observed at 365 and 412 nm.

To verify the effect of high cesium carbonate content on the suppression of Mn^{2+} oxidation, XPS measurements were used to investigate the chemical states of CsMnBr_3 NCs. As shown in Fig. 3b, it is noteworthy that 36.9% of the Mn^{2+} was oxidized to Mn^{3+} in sample S4, which means that Mn^{3+} was produced to strongly absorb the fluorescence. In contrast, there is only Mn^{2+} in sample S7, indicating that the high cesium carbonate content can effectively suppress the oxidation of Mn^{2+} . Therefore, the CO_2 generated by the decomposition of carbonate in the high cesium carbonate content sample could completely eliminate the oxygen in the melt, thereby suppressing the oxidation of Mn^{2+} , so as to realize a significant boost of the PLQY from 2.9% to 65.1% for CsMnBr_3 NCs.

On the basis of this general theory of d-ion emission, the strength of the crystal field defines the position of the Mn^{2+} emission peak: in the weaker field, the ${}^4\text{T}_1$ and ${}^6\text{A}_1$ levels are separated stronger and hence emission occurs at higher energies. As the crystal field increases, the emission peak shifts to lower energies.²⁶ Therefore, the blue shift of PL emission from 663 nm to 649 nm with increasing Cs/Mn ratio is ascribed to the decrease of crystal field strength (Fig. 3c). More importantly, the PL intensity significantly becomes stronger with increasing Cs/Mn ratio, which is mainly ascribed to the increase of CsMnBr_3 NCs and the decrease of Mn^{3+} . In addition, the decrease of crystal-field strength would weaken the energy transfer among Mn^{2+} ions due to weak interaction, so the energy of radiative transition is increased, thus enhancing the PL intensity. As expected, with the increase of Cs/Mn molar ratio, the PLQY initially increases from 2.9% (S4) to 5.1% (S5) to 46.2% (S6) and 65.1% (S7), and then decreases to 54% (S8) (Fig. 3d). The enhancement of PLQY is obviously stronger than that of PL intensity, which may be due to the strong absorption of Mn^{3+} at 412 nm. As shown in Fig. S3,† the photoluminescence decay curves of CsMnBr_3 NCs can be well fitted by a double-exponential function, yielding two lifetimes ($t_1 = 1.16 \mu\text{s}$ and $t_2 = 11.55 \mu\text{s}$) with an average lifetime of $5.92 \mu\text{s}$ (S4), while the PL decay prolongs to $6.37 \mu\text{s}$ ($t_1 = 1.38 \mu\text{s}$ and $t_2 = 17.32 \mu\text{s}$) for S7, which can be ascribed to the decreased nonradiative recombination at a high Cs/Mn ratio.

Then, the effect of halide on the optical properties of Mn^{2+} in these samples was studied, as shown in Fig. 4. The emission peak of CsMnX_3 NC embedded glasses shifts from 645 nm ($\text{X} = \text{I}$) to 649 nm ($\text{X} = \text{Br}$) to 651 nm ($\text{X} = \text{Cl}$), indicating that halide doesn't affect the coordination state of manganese ions in our work. The red-shift of the emission peak is ascribed to the increase in crystal-field strength.^{26,42} The PLQY of CsMnCl_3 and CsMnI_3 NC samples is 48.5% and 33.3%, respectively. As shown in Fig. 4d, the photoluminescence lifetime increases from 4.88 μs to 6.87 μs from I to Cl, which is consistent with a previous report.²⁶

It is worth noting that the high stability of perovskite materials is of great importance for its optoelectronic applications. Therefore, the stability of the CsMnBr_3 NC embedded glasses, including thermal stability and water resistance, is

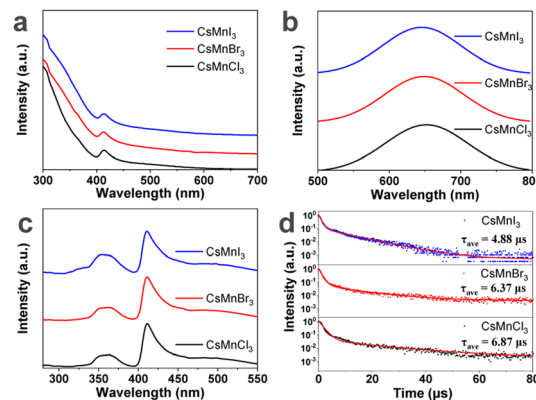


Fig. 4 (a) The UV-vis absorption spectra, (b) PL emission spectra excited at 410 nm, (c) PL excitation spectra with emission monitored at 650 nm, and (d) PL lifetime decay curves of a series of CsMnX_3 ($\text{X} = \text{I}, \text{Br}, \text{Cl}$) NC embedded glass samples.

systematically investigated, as shown in Fig. 5. The temperature dependent (a cycle consisting of heating and cooling) PL spectra of CsMnBr_3 NC embedded glasses from 25 to 200 $^{\circ}\text{C}$ with a step interval of 25 $^{\circ}\text{C}$ are shown in Fig. S4.† Upon heating, the peak emission of CsMnBr_3 NC embedded glasses shows a blue-shift from 649 to 636 nm and the PL intensity gradually decreases. The blue shift can be ascribed to the fact that the lattice expansion leads to a decrease in the crystal field intensity, and crystal expansion results in a decrease in the spin-spin coupling energy between local adjacent Mn^{2+} ions.⁴³ The decrease of luminescence intensity is ascribed to that the increase in temperature will also enhance the interaction between the exciton and phonon and quench the exciton. When the CsMnBr_3 NC embedded glass samples are heated up to 100 $^{\circ}\text{C}$, 81% of the initial PL intensities remained (Fig. 5a). However, for CsPbBr_3 NC embedded glasses samples, only 35% of the initial PL intensity remains at 100 $^{\circ}\text{C}$. These results show that CsMnBr_3 NC embedded glass specimens are highly resistant to thermal quenching. During the cooling process, the emission peak and intensity gradually returned to their original state after one cycle (Fig. 5a and S4†), demonstrating that borosilicate glass provides good protection to CsMnBr_3 NCs and that no degradation is observed within the temperature range of the study.

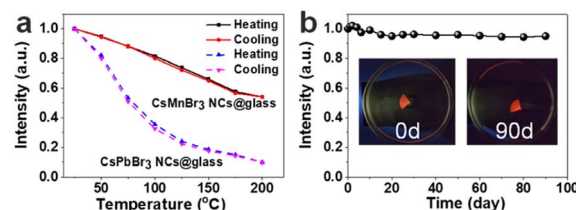


Fig. 5 The stability of CsMnBr_3 NC embedded glasses. (a) Relative intensity for the CsMnBr_3 NCs@glass and CsPbBr_3 NCs@glass sample in the temperature range of 25–200 $^{\circ}\text{C}$. (b) Relative intensity for the CsMnBr_3 NCs@glass sample after soaking in water for different times. Inset shows photographs of CsMnBr_3 NC embedded glasses soaking in water under UV light for 0 and 90 days.



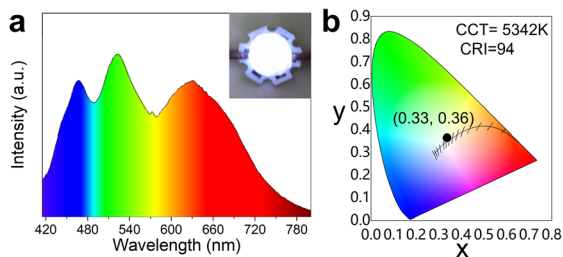


Fig. 6 (a) PL emission spectrum of a 375 nm UV-LED excited white LED device containing the as-synthesized bright and broad red-emissive CsMnBr_3 NC embedded glasses, commercially-available blue-emissive $\text{BaMgAl}_{10}\text{O}_{17}:\text{Eu}^{2+}$ phosphor, and home-made green-emissive $(\text{C}_5\text{H}_6\text{N})_2\text{MnBr}_4$ phosphor. Inset is the lighted photograph of the WLEDs. (b) The CIE chromaticity coordinates of the white LED device shown in (a).

The CsMnBr_3 NC embedded glass sample was immersed in deionized water to simulate a harsh environment and test the water stability. After soaking in water for 90 days, 95% of the initial PL intensity was still maintained (Fig. 5b and S5†), indicating that CsMnBr_3 NCs in these glass specimens are quite stable. As described above, these results clearly demonstrate that the glass encapsulation is robust and prevents CsMnBr_3 NCs from degradation in harsh environments (Table S1†).

The obtained lead-free CsMnBr_3 NC embedded glasses exhibited broad red emission with a high PLQY of 65.1% and excellent stability, making them promising for solid-state lighting applications. For this purpose, we fabricated proof-of-concept WLED devices by encapsulating bright-red-emissive CsMnBr_3 NC embedded glasses, blue-emissive $\text{BaMgAl}_{10}\text{O}_{17}:\text{Eu}^{2+}$, and green-emissive $(\text{C}_5\text{H}_6\text{N})_2\text{MnBr}_4$ phosphor onto a 375 nm LED chip. The obtained WLED displayed white emission with CIE coordinates of (0.33, 0.36) and an excellent CRI value of 94 at a correlated color temperature value of 5342 K (Fig. 6).

Conclusions

In summary, a series of lead-free CsMnX_3 ($\text{X} = \text{Cl}, \text{Br}$, and I) nanocrystals were successfully synthesized in glasses by a high-temperature solid-state method. The oxidation of Mn^{2+} into Mn^{3+} in the melt was prevented by increasing the content of cesium carbonate, so as to realize a significant boost of the PLQY from 2.9% to 65.1%. In the meantime, the transparency of the samples in the 450–700 nm region was also greatly improved. More importantly, cesium manganese halide nanocrystal embedded glasses exhibit outstanding long-term stability in water owing to the dense glass network. As the reported NCs have a high PLQY of 65.1% and large full-width-at-half-maximum (FWHM) of 130 nm, the reported NCs in the current work are particularly suitable as a red fluorescent material for white LED lighting. Thus, using the stable CsMnBr_3 NC embedded glasses as the red emitting material, white light-emitting diodes with CIE coordinates of (0.33, 0.36) and a high color rendering index value of 94 were obtained. This study provided a novel approach for highly bright and stable CsMnX_3

NC embedded glasses, which could eventually advance the applications of metal halide perovskites. By a suitable choice of raw chemical sources and synthetic parameters, it is reasonable to predict that with the current synthesis method for CsMnX_3 NCs the procedures for making white LEDs can be extended to the preparation of other high-performance and stable lead-free perovskite NCs for solid-state lighting.

Experimental

Chemicals

Silica (SiO_2 , 99%, Aladdin), boron oxide (B_2O_3 , 98%, Aladdin), zinc oxide (ZnO , 99%, Aladdin), cesium carbonate (Cs_2CO_3 , 99.9%, Aladdin), manganese carbonate (MnCO_3 , 99.95%, Aladdin), and sodium bromide (NaBr , 99%, Sinopharm), sodium iodide (NaI , 99.5%, Aladdin), sodium chloride (NaCl , 99.5%, Aladdin), and lead bromide (PbBr_2 , 99%, Aladdin).

Preparation of CsMnX_3 NC embedded glass samples

Glass samples with nominal compositions (in mol%) of $15\text{SiO}_2-30\text{B}_2\text{O}_3-10\text{ZnO}-1\text{Cs}_2\text{CO}_3-1\text{MnCO}_3-x\text{NaBr}$ ($x = 5, 7.5, 10, 12.5$, denoted as S1, S2, S4, S3), $15\text{SiO}_2-30\text{B}_2\text{O}_3-10\text{ZnO}-x\text{Cs}_2\text{CO}_3-1\text{MnCO}_3-10\text{NaBr}$ ($x = 1, 1.5, 1.75, 2, 2.25$, denoted as S4, S5, S6, S7, S8), $15\text{SiO}_2-30\text{B}_2\text{O}_3-10\text{ZnO}-2\text{Cs}_2\text{CO}_3-1\text{MnCO}_3-10\text{NaX}$ ($\text{X} = \text{I}, \text{Cl}$), and $15\text{SiO}_2-30\text{B}_2\text{O}_3-10\text{ZnO}-2\text{Cs}_2\text{CO}_3-10\text{NaBr}$ (denoted as blank group) were prepared by a high temperature solid-state chemistry method. The starting materials were carefully weighed according to the stoichiometric proportion and then ground in an agate mortar for half an hour. Subsequently, the mixed powder of about 10 g was placed in a corundum crucible, transferred to a muffle furnace at 1150 °C and allowed to melt for 15 min. Then, the melt was put into a graphite mold, and then the CsMnX_3 NC embedded glass composites were obtained. $(\text{C}_5\text{H}_6\text{N})_2\text{MnBr}_4$ was prepared according to a previous report by our group.²⁷

Characterization

Transmission electron microscopy (TEM) was performed using a JEOL JEM-2800 operating at 200 kV. X-ray photoelectron spectroscopy (XPS) measurements were performed using an achromatic Al K α source (1486.6 eV) and a double pass cylindrical mirror analyzer (ULVAC-PHI 5000 Versa Probe). Ultraviolet and visible (UV-vis) absorption spectra were measured using a Shimadzu UV-3600 plus spectrophotometer at room temperature. Photoluminescence (PL), photoluminescence excitation (PLE) and absolute photoluminescence quantum yield (PLQY) measurements were carried out using a Horiba PTI Quanta Master 400 steady-state fluorescence system with an integrated sphere and double checked with a Hamamatsu Photonics Quantaaurus-QY (model: C11347-11) under ambient conditions. Time-resolved photoluminescence lifetime was detected using an Edinburgh FLS980 spectrometer at room temperature. The photoelectric properties, including the emission spectra, correlated color temperature (CCT), color rendering index (CRI) and International Commission on illumination (CIE) color coordinates of LED devices were collected on an integrating sphere spectroradiometer system (LED300 + HAAS2000, Everfine).



Data availability

Experimental data is described in the ESI,[†] including spectroscopic data.

Author contributions

G. X. designed and performed experiments, and drafted the manuscript. G. X., C. W., Y. L., B. X., W. M., M. P., and G. L. carried out the characterization, and analysed the results. Z. D. supervised the project. All the authors contributed to the discussion during the whole project.

Conflicts of interest

There are no conflicts to declare.

Acknowledgements

This work was supported by the National Natural Science Foundation of China (22075129).

Notes and references

- 1 Y. Hassan, J. H. Park, M. L. Crawford, A. Sadhanala, J. Lee, J. C. Sadighian, E. Mosconi, R. Shivanna, E. Radicchi, M. Jeong, C. Yang, H. Choi, S. H. Park, M. H. Song, F. De Angelis, C. Y. Wong, R. H. Friend, B. R. Lee and H. J. Snaith, *Nature*, 2021, **591**, 72–77.
- 2 X. Li, X. Gao, X. Zhang, X. Shen, M. Lu, J. Wu, Z. Shi, V. L. Colvin, J. Hu, X. Bai, W. W. Yu and Y. Zhang, *Adv. Sci.*, 2021, **8**, 2003334.
- 3 Q. Zhang, Q. Shang, R. Su, T. T. H. Do and Q. Xiong, *Nano Lett.*, 2021, **21**, 1903–1914.
- 4 Y. Guo, F. Gao, P. Huang, R. Wu, W. Gu, J. Wei, F. Liu and H. Li, *Energy Mater. Adv.*, 2022, 9857943.
- 5 L. Manna, O. M. Bakr, S. Brovelli and H. Li, *Energy Mater. Adv.*, 2022, 9865891.
- 6 Y. Zhao and K. Zhu, *Chem. Soc. Rev.*, 2016, **45**, 655–689.
- 7 M. V. Kovalenko, L. Manna, A. Cabot, Z. Hens, D. V. Talapin, C. R. Kagan, V. I. Klimov, A. L. Rogach, P. Reiss, D. J. Milliron, P. Guyot-Sionnest, G. Konstantatos, W. J. Parak, T. Hyeon, B. A. Korgel, C. B. Murray and W. Heiss, *ACS Nano*, 2015, **9**, 1012–1057.
- 8 L. Protesescu, S. Yakunin, M. I. Bodnarchuk, F. Krieg, R. Caputo, C. H. Hendon, R. X. Yang, A. Walsh and M. V. Kovalenko, *Nano Lett.*, 2015, **15**, 3692–3696.
- 9 F. Zhang, H. Zhong, C. Chen, X.-g. Wu, X. Hu, H. Huang, J. Han, B. Zou and Y. Dong, *ACS Nano*, 2015, **9**, 4533–4542.
- 10 M.-G. Ju, M. Chen, Y. Zhou, J. Dai, L. Ma, N. P. Padture and X. C. Zeng, *Joule*, 2018, **2**, 1231–1241.
- 11 Y. Zhou and Y. Zhao, *Energy Environ. Sci.*, 2019, **12**, 1495–1511.
- 12 S. Zou, Y. Liu, J. Li, C. Liu, R. Feng, F. Jiang, Y. Li, J. Song, H. Zeng, M. Hong and X. Chen, *J. Am. Chem. Soc.*, 2017, **139**, 11443–11450.
- 13 B. A. Koscher, J. K. Swabeck, N. D. Bronstein and A. P. Alivisatos, *J. Am. Chem. Soc.*, 2017, **139**, 6566–6569.
- 14 S. Chang, Z. Bai and H. Zhong, *Adv. Opt. Mater.*, 2018, **6**, 1800380.
- 15 F. Gao, J. Wu, Y. Zhao, T. Song, Z. Deng, P. Wang, Y. Wang and H. Li, *Nanoscale*, 2021, **13**, 10329–10334.
- 16 Y. Zeng, W. Chen, Y. Deng, W. Gu, C. Wu, Y. Guo, P. Huang, F. Liu and H. Li, *ACS Appl. Nano Mater.*, 2022, **5**, 9534–9543.
- 17 X. Pang, S. Si, L. Xie, X. Zhang, H. Huang, S. Liu, W. Xiao, S. Wang, T. Xuan, J. Zhuang, C. Hu, Y. Liu, B. Lei and H. Zhang, *J. Mater. Chem. C*, 2020, **8**, 17374–17382.
- 18 Y. Ye, W. Zhang, Z. Zhao, J. Wang, C. Liu, Z. Deng, X. Zhao and J. Han, *Adv. Opt. Mater.*, 2019, **7**, 1801663.
- 19 X. Xiang, H. Lin, J. Xu, Y. Cheng, C. Wang, L. Zhang and Y. Wang, *Chem. Eng. J.*, 2019, **378**, 122255.
- 20 Z. Li, Z. Deng, A. Johnston, J. Luo, H. Chen, Y. Dong, R. Sabatini and E. H. Sargent, *Adv. Funct. Mater.*, 2022, **32**, 2111346.
- 21 F. Wang, J. Ma, F. Xie, L. Li, J. Chen, J. Fan and N. Zhao, *Adv. Funct. Mater.*, 2016, **26**, 3417–3423.
- 22 X. Wu, W. Song, Q. Li, X. Zhao, D. He and Z. Quan, *Chem.–Asian J.*, 2018, **13**, 1654–1659.
- 23 P. Gao, S. Cheng, J. Liu, J. Li, Y. Guo, Z. Deng, T. Qin and A. Wang, *Molecules*, 2022, **27**, 8259.
- 24 Y. Li, C. Wang, G. Hu, W. Meng, S. Sui and Z. Deng, *Chem. Commun.*, 2022, **58**, 941–944.
- 25 Y. Li, C. Wang, G. Xu, G. Luo and Z. Deng, *J. Phys. Chem. Lett.*, 2023, **14**, 2006–2011.
- 26 V. Morad, I. Cherniukh, L. Pottschacher, Y. Shynkarenko, S. Yakunin and M. V. Kovalenko, *Chem. Mater.*, 2019, **31**, 10161–10169.
- 27 G. Hu, B. Xu, A. Wang, Y. Guo, J. Wu, F. Muhammad, W. Meng, C. Wang, S. Sui, Y. Liu, Y. Li, Y. Zhang, Y. Zhou and Z. Deng, *Adv. Funct. Mater.*, 2021, **31**, 2011191.
- 28 Q. Kong, B. Yang, J. Chen, R. Zhang, S. Liu, D. Zheng, H. Zhang, Q. Liu, Y. Wang and K. Han, *Angew. Chem., Int. Ed.*, 2021, **60**, 19653–19659.
- 29 T. W. Kang, E. J. Choi, Y. J. Park, J. Hwang, B. Bae and S. W. Kim, *Opt. Lett.*, 2022, **47**, 1806–1809.
- 30 H. Yuan, F. Massuyeau, N. Gautier, A. B. Kama, E. Faulques, F. Chen, Q. Shen, L. Zhang, M. Paris and R. Gautier, *Angew. Chem., Int. Ed.*, 2020, **59**, 2802–2807.
- 31 W. F. Zhang, W. J. Pan, T. Xu, R. Y. Song, Y. Y. Zhao, C. Y. Yue and X. W. Lei, *Inorg. Chem.*, 2020, **59**, 14085–14092.
- 32 H. Xiao, P. Dang, X. Yun, G. Li, Y. Wei, Y. Wei, X. Xiao, Y. Zhao, M. S. Molokeev, Z. Cheng and J. Lin, *Angew. Chem., Int. Ed.*, 2021, **60**, 3699–3707.
- 33 K. Li, W. Zhang, L. Niu, Y. Ye, J. Ren and C. Liu, *Adv. Sci.*, 2023, **10**, 2204843.
- 34 M. Czaja, R. Lisiecki, A. Chrobak, R. Sitko and Z. Mazurak, *Phys. Chem. Miner.*, 2017, **45**, 475–488.
- 35 Z. Chen, Q. Wang, Y. Tong, X. Liu, J. Zhao, B. Peng, R. Zeng, S. Pan, B. Zou and W. Xiang, *J. Phys. Chem. Lett.*, 2022, **13**, 4701–4709.
- 36 J. Almutlaq, W. J. Mir, L. Gutiérrez-Arzaluz, J. Yin, S. Vasylevskyi, P. Maity, J. Liu, R. Naphade,



- O. F. Mohammed and O. M. Bakr, *ACS Mater. Lett.*, 2021, **3**, 290–297.
- 37 K. Li, Y. Ye, W. Zhang, Y. Zhou, Y. Zhang, S. Lin, H. Lin, J. Ruan and C. Liu, *Nano Res.*, 2022, **15**, 9368–9376.
- 38 H. M. Pan, Q. L. Yang, X. X. Xing, J. P. Li, F. L. Meng, X. Zhang, P. C. Xiao, C. Y. Yue and X. W. Lei, *Chem. Commun.*, 2021, **57**, 6907–6910.
- 39 C. Vancea, G. Mosoarca and S. Popa, *Int. J. Environ. Res. Public Health*, 2021, **18**, 6585.
- 40 H. Bahmani Jalali, A. Pianetti, J. Zito, M. Imran, M. Campolucci, Y. P. Ivanov, F. Locardi, I. Infante, G. Divitini, S. Brovelli, L. Manna and F. Di Stasio, *ACS Energy Lett.*, 2022, **7**, 1850–1858.
- 41 B. Su, G. Zhou, J. Huang, E. Song, A. Nag and Z. Xia, *Laser Photonics Rev.*, 2021, **15**, 2000334.
- 42 D. J. Newman, *Aust. J. Phys.*, 1977, **30**, 315–324.
- 43 X. Hao, H. Liu, W. Ding, F. Zhang, X. Li and S. Wang, *J. Phys. Chem. Lett.*, 2022, **13**, 4688–4694.

